International Journal of Plasticity 138 (2021) 102942

Contents lists available at ScienceDirect

International Journal of Plasticity

journal homepage: http://www.elsevier.com/locate/ijplas

On the origin of microstructural discontinuities in sliding contacts: A discrete dislocation plasticity analysis

Yilun Xu [a,b,**], Friederike Ruebeling [c,d], DanielS. Balint [a], Christian Greiner [c,d], Daniele Dini [a,*]

[a] Department of Mechanical Engineering, Imperial College London, South Kensington Campus, Exhibition Road, London, SW7 2AZ, UK
[b] Department of Materials, Imperial College London, South Kensington Campus, Exhibition Road, London, SW7 2AZ, UK
[c] Karlsruhe Institute of Technology (KIT), Institute for Applied Materials (IAM), Kaiserstrasse 12, 76131, Karlsruhe, Germany
[d] KIT IAM-CMS MicroTribology Center (μTC), Strasse am Forum 5, 76131, Karlsruhe, Germany

ARTICLE INFO

Keywords:
Sliding
Discrete dislocation plasticity
Lattice rotation
Size effect

ABSTRACT

Two-dimensional discrete dislocation plasticity (DDP) calculations that simulate single crystal films bonded to a rigid substrate under sliding by a rigid sinusoid-shaped asperity are performed with various contact sizes. The contact between the thin film and the asperity is established by a preceding indentation and modelled using a cohesive zone method (CZM), whose behavior is governed by a traction-displacement relation. The emergence of microstructural changes observed in sliding tests has been interpreted as a localized lattice rotation band produced by the activity of dislocations underneath the contact. The depth of the lattice rotation band is predicted to be well commensurate with that observed in the corresponding tests. Furthermore, the dimension and magnitude of the lattice rotation band have been linked to the sliding distance and contact size. This research reveals the underpinning mechanisms for the microstructural changes observed in sliding tests by explicitly modelling the dislocation patterns and highly localized plastic deformation of materials under various indentation and sliding scenarios.

1. Introduction

Microstructure determines the material performance under contact, including but not limited to hardness (Chenje et al., 2004), coefficient of friction (COF) (Rigney and Hirth, 1979), anti-fretting (Zhang et al., 2009) and wear resistance (Rigney and Glaeser, 1978) under a tribological loading condition, particularly when the contact size approaches the grain size. Correspondingly, the subsurface microstructure of specimens is simultaneously changed by the plasticity induced by external tribological load that couples normal and tangential components. Therefore, it is significant to understand the mechanisms of the mutual interactions between the microstructure and the local deformation of materials under tribology loadings. Among complex tribology loading scenarios, the single asperity sliding problem provides an elementary mechanistic benchmark for revealing the mechanisms for microstructure change.

The phenomenon of microstructure variation in the sample subsurface under tribological loads has commonly been observed in experimental studies *e.g* (Hattori et al., 2008; Hughes and Hansen, 2001; Stoyanov et al., 2014). on various crystalline metals,

* Corresponding author.
** Corresponding author. Department of Mechanical Engineering, Imperial College London, South Kensington Campus, Exhibition Road, London, SW7 2AZ, UK.
E-mail addresses: yilun.xu@imperial.ac.uk (Y. Xu), d.dini@imperial.ac.uk (D. Dini).

https://doi.org/10.1016/j.ijplas.2021.102942
Received 17 November 2020; Received in revised form 16 January 2021; Accepted 20 January 2021
Available online 30 January 2021
0749-6419/© 2021 The Authors. Published by Elsevier Ltd. This is an open access article under the CC BY-NC-ND license (http://creativecommons.org/licenses/by-nc-nd/4.0/).

including nickel, copper and aluminum. Numerical investigations including the work (Karthikeyan et al., 2009; Pastewka et al., 2011) were performed to understand the intrinsic mechanisms of the subsurface modification under sliding. However, due to the complexity of the tribology contact loads, neither of the experimental nor numerical studies have not yet elucidated the phenomenon with satisfactory mechanisms. A more recent experimental study (Greiner et al., 2016) using Scanning Transmission Electron Microscopy (STEM) has shown a "dislocation traceline", *i.e.* an apparent contrast change in the STEM images within the subsurface of a copper specimen after one-stroke sliding. The abrupt contrast change was interpreted as a special dislocation piling up pattern under the contact and serves as a key mechanistic driver giving rise to subgrain boundary formation and further damage in subsequent cyclic tribological loading (Greiner et al., 2016).

There are no physics-based mechanisms that have yet been proposed to provide a convincing insight for the emergence of tracelines observed in sliding tests. In order to interpret microstructural changes observed in the subsurface during sliding tests, a previous study (Greiner et al., 2018) employed a continuum model to describe the dislocation activity by assessing the inhomogeneous stress field variation under the moving indenter. However, due to the lack of a length scale parameter and the discrete nature of the phenomenon under investigation, neither conventional continuum approaches nor crystal plasticity (*e.g.* (Dunne et al., 2007b)) is capable of capturing the highly localized and discrete deformation observed in the experiments. It is in fact more sensible to explicitly model dislocation activities that appear to be likely responsible for the microstructural discontinuities. Hence, a 2D Discrete Dislocation Plasticity (DDP) model is established in this paper to simulate the evolution of dislocations motion and their pile up pattern under the sliding. The DDP numerical framework has been extensively applied to provide microstructure- and length-scale associated interpretation to a variety of fundamental micromechanical problems, including tension (Balint et al., 2008), micro-compression (Akarapu et al., 2010), bending (Prastiti et al., 2020; Tarleton et al., 2015), nano-indentation (Qu et al., 2006) and pure sliding (Deshpande et al., 2004) by simulating the activity of individual dislocations that is governed by nucleation, mobility and pinning laws. In this framework, the material behavior is completely determined by the collective activities of dislocations under contact. The contact between the specimen and indenter that is established by a preceding sinusoidal micro-indentation is modelled using a cohesive zone method (CZM), whose shear stress performance is governed by a non-soften traction-displacement relation (Deshpande et al., 2007). We herein aim to investigate the underpinning mechanisms for local microstructural deformation and the induced lattice rotation under single asperity sliding using the DDP framework integrated with experimental observations (Ruebeling et al., 2021). The numerical results shed light on the mechanisms for the emergence of the dislocation tracelines observed in the experiment by explicitly illustrating the activity of dislocations immediately under the contact, the evolution of geometrically necessary dislocations (GND) and the consequent localized lattice rotation of the subsurface under various indentation and sliding scenarios. In addition, this research also provides a pioneering framework for simulating the localized deformation and the subsequent microstructural changes observed in multi-cycle tribological tests, *e.g.* shown in the work (Greiner et al., 2016). The results of the analysis also benefit researchers and engineers in their pursuit of tailoring and optimizing the anti-wear properties of materials and coatings.

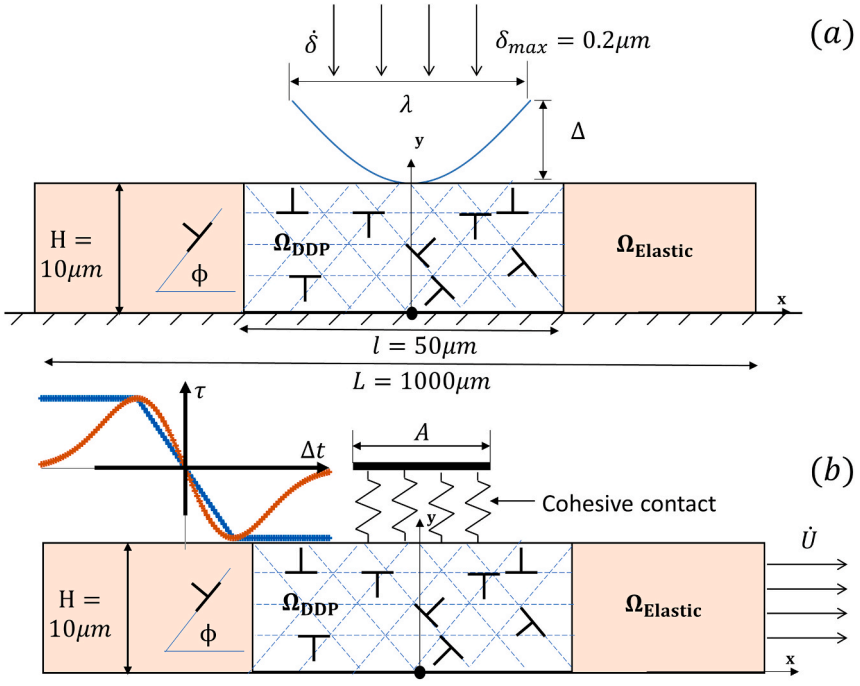

Fig. 1. Schematic illustration of (a) the sinusoidal indentation and (b) the subsequent monotonic sliding boundary value problem, solved using the DDP model.

2. Methodology

2.1. Discrete dislocation plasticity formulation

We herein employ the classical two-dimensional, plane strain, isotropic discrete dislocation plasticity (DDP) computational framework first described by Van der Giessen and Needleman (Van der Giessen and Needleman, 1995). Although three-dimensional discrete dislocation plasticity (3D-DDD) could also be used to improve our understanding of material deformation (*e.g.* (Bertin et al., 2020; El Ters and Shehadeh, 2019; Gurrutxaga-Lerma et al., 2017; Lu et al., 2019; Motz et al., 2008)), the 2D DDP framework reflects important dislocation-related features of crystalline materials (van der Giessen et al., 2020), which can be more swiftly used to explore fundamental aspects of permanent deformations and irreversible changes. The 2D DDP framework adopted in this paper explicitly simulates the nucleation, glide, pinning and interaction of the edge components of individual dislocation loops in crystals subject to external loads and constraints assuming plane strain conditions. The formulation exploits Bueckner's principle to represent the collective effect of dislocations by their linear elastic superposition; plasticity arises from the irreversible, quasi-static evolution of the elastic fields associated with all dislocations in the system. Hence, the localized micromechanical behavior of crystalline materials (*e.g.* stress, strain and slip etc.) are calculated based on the instantaneous dislocation structure induced by various loading scenarios, such as tension (Balint et al., 2006b), indentation (Lu et al., 2019), shock and high strain rate loading (Gurrutxaga-Lerma et al., 2017; Gurrutxaga–Lerma et al., 2020), and cyclic loading (Xu et al., 2020). The essential details of the DDP framework have been given in (Balint et al., 2005); only the aspects of the DDP formulation that are distinct from the basic recipe are described here.

2.2. The DDP model setup for sliding

The basic DDP model described above is adapted here for frictional sliding problems. The aim is to use the model to reproduce the experimental observation, hence enable its physical interpretation. An initial sinusoidal indentation process is utilized to establish contact between the rigid asperity and the specimen. This is followed by monotonic sliding with a cohesive zone model (CZM) between the asperity and the specimen (Deshpande et al., 2004).

The specimen is made of a DDP region underneath a sinusoidal asperity with an elastic medium on either side, as depicted in Fig. 1. The DDP *process window* represents a single FCC-like crystal in a plane strain orientation and is assigned with aluminum-like properties. The key material properties adopted here are reported in Table 1, and further details of the DDP parameters associated with this crystal representation can be found in (Xu et al., 2016). Although the crystal representation does not correspond exactly to the pure copper tested in the experiments, the similarity of the slip systems ($\Phi^{(\alpha)} = 0, \pm 45^{\circ}$ with respect to the x-axis in the model) to those in the experiments enables mechanistic study of the microstructural change observed in the sliding tests.

The DDP process window with dimension $l \times h$ is discretized by a finite element mesh (the finite element method is used to solve the correction, or reduced problem of the Bueckner linear superposition) that is highly focused towards the center of the contact area. The finite element mesh is made up of 240 × 100 bi-linear elements with a typical mesh size of $\Delta x = 0.005$ μm in the refined zone, which has dimensions 1 μm × 1 μm. A mesh-size sensitivity study was conducted, and the mesh size mentioned above was found to be an optimal balance between computation expense and numerical accuracy. A sufficiently-small time increment of $\Delta t = 0.5$ns was used to sufficiently resolve the evolution of the dislocation structure.

Although the sinusoidal indentation model invokes a small strain approximation, the contact between the indenter and film is based upon the *deformed* film surface. Indentation depth is denoted by δ, and true contact length A is defined as the distance between the intersections of the indenter surface and the deformed film surface. In general, the true contact length A differs from the nominal contact length as material sink-in or pile-up (Balint et al., 2006a) occurs. Also, nominal contact area does not account for the effect of surface roughness, comprised of steps created by dislocations exiting at the free surface, on the contact area, hence hardness (as analyzed and discussed in (Widjaja et al., 2007a).

The total reaction force of the thin film response to the applied indentation depth is computed as in eq. (1):

$$F = -\int_{-A/2}^{A/2} T_y(x, H)dx \tag{1}$$

where T_y is the surface traction in the y-direction, hence the indentation pressure (*i.e.* instantaneous or indentation depth-dependent hardness) p is defined by:

$$p \equiv F/A \tag{2}$$

where A is the actual, end-to-end length definition of the contact area.

The interaction between surfaces can be modelled by applying a continuum cohesive formula (Johnson, 1997). In the sliding simulations, the interaction between the sinusoidal asperity and the specimen is modelled using a cohesive zone on the contacting surface of length A with a relation between shear traction versus displacement, which is given by:

$$T_t = \begin{cases} -\tau_{max}\dfrac{\Delta t}{\delta_t}, & if \ \ |\Delta t| < \delta_t \\ -\tau_{max} sign(\Delta t), & if \ \ |\Delta t| > \delta_t \end{cases} \tag{3}$$

where $\Delta t = u_x(x,H)$ is the tangential displacement jump across the cohesive surface, and $T_t = T_x$ is the shear traction. Hence, the interaction is a cohesive resistance to the relative sliding of the thin film, here chosen to be represented by a "non-softening" cohesive relation with unbounded shear work of separation (Deshpande et al., 2004). While there is at present no fundamental basis for choosing the form of cohesive relation to use in conjunction with the discrete dislocation description of material behavior, the interaction between adhesion and tangential tractions is in itself currently at the center of an active scientific debate (see *e.g.* (Menga et al., 2018; Peng et al., 2021)) and very much depends on the nature of the specific interfacial characteristics of the contact pair being investigated. In addition, the cohesive law chosen in our study helps the convergence of contact calculations, and hence has been commonly used in other sliding studies, such as (Deshpande et al., 2007; Song et al., 2016).

Traction free boundary conditions are applied on the part of the surface outside of the contact region:

$$T_x = T_y = 0 \ \text{ on } \ x = 0 \notin S_{contact} \ \text{ and } \ y = H \tag{4}$$

The maximum cohesive strength τ_{max} is set to be τ_{max} = 300 MPa and the threshold displacement jump is δ_t = 0.5 nm. The parameter values in the non-softening traction-displacement relation are identical to (Deshpande et al., 2007)).

The displacement rates,

$$\dot{U}_x = \dot{U}, \dot{U}_y = 0 \tag{5}$$

are imposed on the specimen boundaries $x = \pm L/2$, and $y = 0$, to simulate the relative sliding of the specimen with respect to the contact surface with magnitude $\dot{U}/A = 10^4 s^{-1}$ in the positive x-direction. The maximum sliding distance is set as approximately one half of the corresponding contact size A, which is sufficiently large to achieve a full slip condition (see the later discussion in Section 3.2) of the film. The sliding rate $\dot{U}$ was chosen sufficiently low to ensure a quasi-static sliding process, *i.e.* that dislocations are in an equilibrium configuration at any sliding instance, hence the effect of loading rate on sliding (due to nucleation time and mobility as shown in (Song et al., 2016) is negligible. The averaged shear stress τ along the contact is given by:

$$\tau = -\frac{1}{A}\int_{-A/2}^{A/2} T_x(x,H)dx \tag{6}$$

Different from the pure sliding calculations where films are assigned with a dislocation- and stress-free initial state using the DDP framework, *e.g.* (Benzerga, 2008)), the sliding simulations herein start with a certain normal load and actual contact size to accommodate the experimental setup. In fact, this type of sliding calculation is initiated with a deformation field and dislocation structure in the specimen that is introduced from the initial sinusoidal indentation simulations described above, with varying indentation depth.

2.3. Lattice rotation calculation

We use the DDP framework described above to model the microstructural change, more specifically, the elastic lattice rotation within the thin film under frictional sliding scenarios. The lattice rotation is defined as the antisymmetric part of the displacement gradient tensor, which for the planar situation can be expressed in terms of the off-diagonal components of the small strain tenor ε_{ij}. Therefore, lattice rotation is comprised of the derivatives of the displacements in the infinite plane discrete dislocation field and $\widetilde{(\ )}$ and the continuum correction field $\widehat{(\ )}$:

$$\Omega = \frac{1}{2}\left(\widehat{u}_{2,1} + \widetilde{u}_{2,1} - \widehat{u}_{1,2} - \widetilde{u}_{1,2}\right) \tag{7}$$

The DDP model considers only glide of edge type dislocations along predefined slip systems within the material, which introduce slip (displacement discontinuities) across the slip planes. A cluster of dislocations piling up introduces lattice rotation to the material. This phenomenon has also been reported in indentation problems (Balint et al., 2006a; Po et al., 2019; Zhang et al., 2014). Displacement discontinuities should not appear in the derivatives of the displacements, they are continuous, however this requires analytical differentiation. Standard numerical differentiation of the dislocation displacement fields will reveal a discontinuity, a fact that is often exploited for visualization of slip localization (Hirth and Lothe, 1982). Hence when computed in this way, the definition of lattice rotation Ω in eq. (9) naturally excludes slip features from the $\widetilde{(\ )}$ field.

In principle, we can employ a different background mesh, using interpolation, that is different from the finite element mesh used in the calculation in order to change the resolution of field quantities. In this work we resolve field quantities on the highly focused mesh used in the simulation to maintain their spatial resolution in the vicinity of the indentation, especially near the contact surface. The lattice rotation calculation was performed every 100 times increments, *i.e.* $\Delta U/A = 5 \times 10^{-4}$, to capture the temporal evolution of lattice rotation against sliding distance.

The aforementioned elastic lattice rotation method was verified for a wedge-shaped indentation problem; a comparison to prior simulations (such as (Zhang et al., 2014)) is shown in the Appendix (and in Fig. A1). The abrupt change in the sign of the lattice rotation near the midline of the contact is consistent with experimental observations (Kysar et al., 2010) and continuum plasticity analyses (Bouvier and Needleman, 2006). The values of lattice rotation predicted here are also consistent with (Zhang et al., 2014). It is worth noting that the lattice rotation distribution is obtained by the combined effect (linear superposition of fields) of dislocations on the three slip systems, and the lattice rotation caused by isolated dislocations is long range. Therefore, the lattice rotation distribution

shows a different pattern from the corresponding dislocation distribution, since the rotations caused by isolated, moving dislocations is experienced far from the dislocations themselves; in other words, regions with a high value of dislocation density do not necessarily exhibit a hot spot of lattice rotation. This phenomenon is further illustrated and discussed when looking at the evolution of lattice rotation contours and dislocation structure in the following sections (see *e.g.* Fig. 9).

3. Numerical results

3.1. Sinusoidal indentation response

The variation of actual indentation pressure p_A and actual indentation contact area A against applied indentation depth δ under the rigid sinusoidal asperity with an amplitude $\Delta = 0.5\mu m$ and wavelength $\lambda = 10\mu m$ are reported in Fig. 2. The indentation pressure does not exhibit a strong indentation size effect (ISE) response, consistent with micro-indentation tests (Kuksenko et al., 2019; Pharr et al., 2010) and numerical simulations (Balint et al., 2006a; Lewandowski and Stupkiewicz, 2018; Saraev and Miller, 2006), when the indentation depth exceeds $\delta = 0.02\mu m$. The presence of an ISE requires a high strain gradient in the plastically deforming volume under the indenter (Nix and Gao, 1998), accommodated by a high density of geometrical necessary dislocations (GNDs). However, the relatively blunt, smooth surface of the sinusoidal indenter (*e.g.* compared to a wedge) used here suppresses the development of the strain gradient when indentation depth is sufficiently large ($\delta > 0.02\mu m$), and the actual indentation pressure response stabilizes at a plateau level that represents the continuum hardness of the specimen. The hardness value predicted here, $p_A \cong 210$MPa, is reasonably close to the continuum plasticity prediction, $p_A = 3\sigma_Y$, which establishes that plastic flow dominates the specimen response under sinusoidal indentation with a large contact size. The size-insensitive indentation pressure regime is useful in understanding the shear stress response in later sliding calculations by excluding the normal stress interference. Compared to the nominal contact size (dashed line in Fig. 2), the actual contact size systematically exhibits a smaller value by virtue of the material sink-in near the contact, which was observed in prior DDP analyses of indentation (Widjaja et al., 2007b; Xu et al., 2019).

3.2. Subsurface deformation at different stages during sliding

The evolution of the average shear stress τ_{avg} along the contact with the sliding distance U is reported in Fig. 3 using the DDP model. The results were obtained from sliding simulations starting from four different initial indentation depths, $\delta = 0.01, 0.05, 0.10, 0.20\mu m$, with a sinusoidal asperity shape with $\lambda = 10\mu m$ and $\Delta = 0.5\mu m$, and the corresponding actual contact sizes A $= 1.11, 3.55, 5.52, 8.42\mu m$, respectively, were achieve by the initial indentation. Following an initial linear response, the evolution curves continue to increase but with a much slower and strongly contact size dominated rate $\partial\tau/\partial$A until the cohesive strength τ_{max} is achieved. It can be observed that the critical sliding distance for the average shear stress achieving the cohesive strength depends on the contact size. In previous studies on sliding calculations without a prior indentation, the shear stress was found to be inversely square root dependent on the contact size (Deshpande et al., 2007). The preceding sinusoidal indentation in this research introduces considerable plasticity into the film prior to the sliding, therefore the relationship revealed under pure sliding does not hold when indentation is first applied. The quantitative relation between the shear stress increase with the initial indentation and the contact size will be investigated in detail in future studies.

The total dislocation density ρ_{dis} (number of dislocations divided by the area of the dislocation process window) evolution with the sliding distance U is reported in Fig. 4, where results were obtained from the aforementioned DDP simulations for four different contact sizes. The total dislocation density linearly increases from a base value that was inherited from the preceding indentation. The rate of increase in the dislocation density is found to be independent of contact size.

After a critical sliding distance, the rate of increase is reduced for all contact sizes, when more plasticity is introduced into the specimen by virtue of the increased sliding load; the critical sliding distance at which this occurs strongly depends on the contact size, and is greater than the critical sliding distance at which the average shear stress achieves the cohesive strength for a given contact size

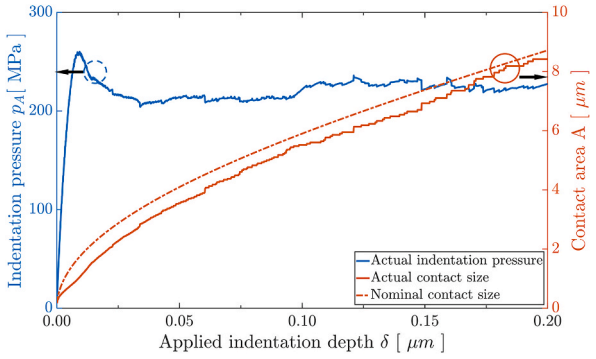

Fig. 2. Actual indentation pressure p_A and actual contact size A versus applied indentation depth δ by the sinusoidal asperity with $\lambda = 10\mu m$ and $\Delta = 0.5\mu m$. The nominal contact size A_N (denoted by the dash-dot line) response is also included for comparison.

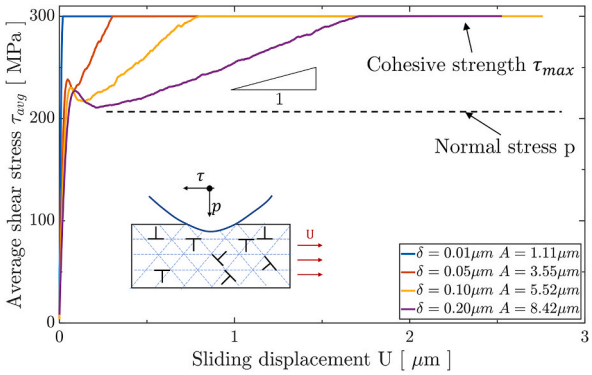

Fig. 3. Shear stress τ evolution with sliding displacement U for four different contact sizes that are introduced by initial sinusoidal indentation. The normal stress p and cohesive strength τ_{max} are denoted for reference.

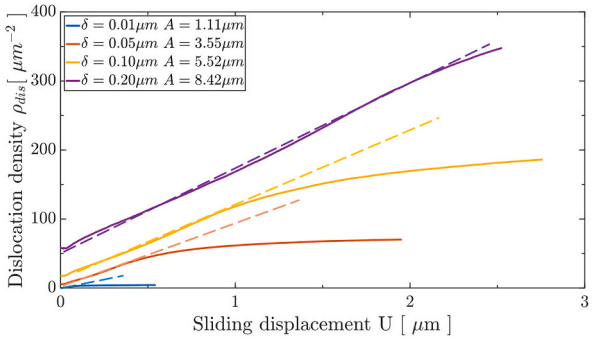

Fig. 4. Total dislocation density ρ_{dis} evolution against sliding displacement U under different contact sizes introduced by an initial sinusoidal indentation. The dashed lines indicate the contact-size independent dislocation density increase rate prior to full slip occurring.

(see Fig. 3). For instance, the critical sliding distances are predicted as 1.0μm and 0.76μm for the dislocation density evolution and shear stress evolution, respectively, for a contact size A = 5.52μm. The dislocation density eventually reaches a plateau value (except for the largest contact size A = 8.42μm), which is determined by the contact size, and ceases to increase with sliding distance. This suggests that the film is saturated by a stable dislocation structure, therefore full slip between the contact and specimen occurs.

Hence, three different sliding stages are identified, demarcated by the two aforementioned critical sliding distances for a given contact size. While the average shear stress evolution reflects plastic flow due to dislocation activity within the surface region (Deshpande et al., 2004, 2005) only, the dislocation density evolution is able to identify the point at which the full slip state initiates, *i.e.* when the dislocation structure and deformation field within the entire specimen reach a dynamic equilibrium and the dislocation density tends to saturate as sliding takes place. In the following sections, lattice rotation maps in the whole specimen are analyzed at different sliding stages for various contact sizes.

3.3. Lattice rotation evolution during sliding

The lattice rotation is calculated using eq. (9) according to the dislocation structure and deformation field at a certain instant of a sliding process. The evolution of the lattice rotation distribution for the contact size A = 3.55 μm for single-stroke (left to right) sliding is illustrated in Fig. 5 with individual dislocations shown explicitly as black marks; a view of the entire specimen is shown above a close-up view of the 10μm × 1μm dashed region shown. With increase in sliding distance the lattice rotation accumulates underneath and behind the contact. In particular, it is shown that the lattice rotation introduced by the indentation that precedes sliding is negligible compared to that induced by the sliding itself. As shown in (c) and (d), after sufficient sliding the lattice rotation in a thin layer of material immediately underneath the contact with thickness $h^* \approx 100$ nm has its lattice rotation 'locked in', i.e. it does not increase in intensity but does spread with further sliding.

This is accompanied by localization of lattice rotation in a thin band beneath this layer, which spreads parallel to the sliding direction and increases in strength as the sliding distance increases. More bands of localized lattice rotation with associated 'locked-in' layers are visible with increasing distance below the surface, particularly once the full sliding conditions are achieved (Fig. 5(d)). The 'locked-in' lattice rotation bands correspond to the trace lines experimentally observed in (Greiner et al., 2016, 2018), where the localization band is the boundary between them.

Lattice rotation within a single crystal material is associated with the presence of geometrically necessary dislocations (GNDs)

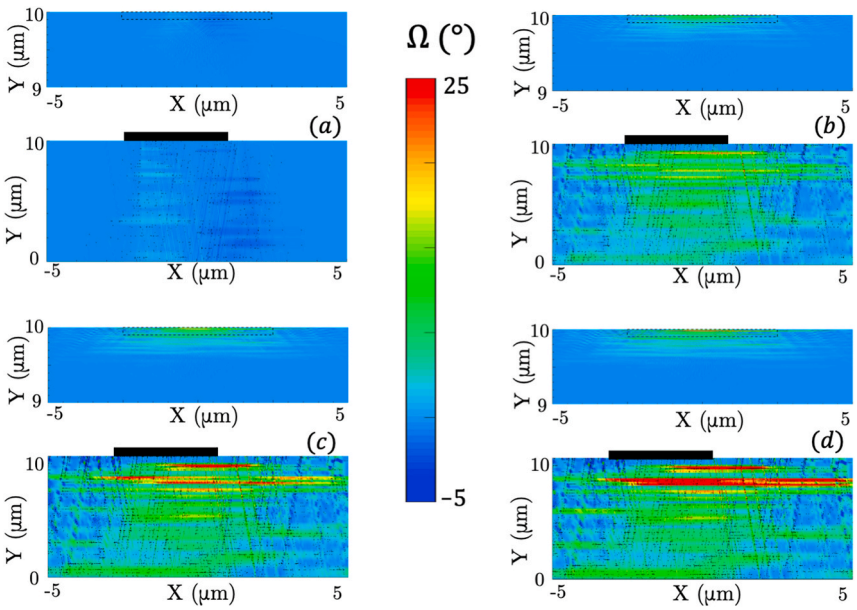

Fig. 5. The contours of lattice rotation Ω and the corresponding dislocation structures (individual dislocations represented as black dots) of the sliding calculation starting from $\delta = 0.05$ μm and $A = 3.55$ μm. Results are shown for sliding distances (a) $U = 0$ (i.e. just after indentation), (b) $U = 0.497$ μm (the initial slip), (c) $U = 1.561$ μm (partial slip) and (d) $U = 1.953$ μm (full sliding), where U is the relative surface displacement, A the contact size and δ the indentation depth. The set of lattice rotation contours with corresponding dislocation structures illustrate the emergence of the 'locked-in' and localized lattice rotation bands during the sliding process.

(Arsenlis and Parks, 1999), microstructure change (Cheng and Ghosh, 2015; Cheong et al., 2005; Das et al., 2018; Dunne et al., 2007a) and non-local effect (Counts et al., 2008; Meissonnier et al., 2001). The results shown in the following sections correspond to sliding distances that exceed that required for the full sliding condition, beyond which the layered lattice rotation distribution depicted in Fig. 5 is fully developed.

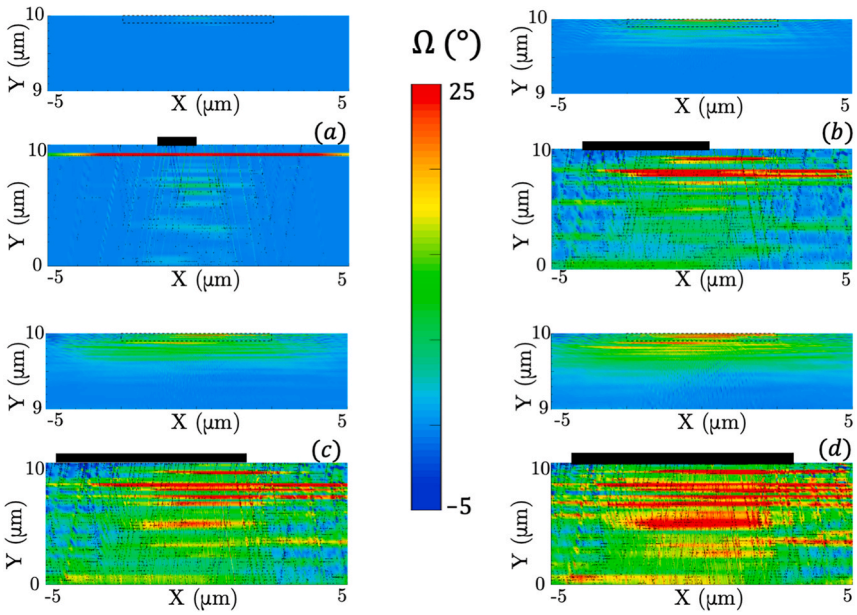

Fig. 6. The contours of lattice rotation Ω and the corresponding dislocation structure (individual dislocations represented as black dots) of the sliding calculation obtained for different contact sizes. (a) A = 1.11 μm, (b) A = 3.55 μm, (c) A = 5.52 μm and (d) A = 8.42 μm, where U is the displacement, A the contact size and δ the indentation depth. Results are shown at the instants where full sliding has been achieved for each contact size and the indenter has moved away from the initial contact area (a, b and c), or for the maximum sliding distance the calculation has reached (d). The set of lattice rotation contours illustrates the lattice rotation bands formed during sliding and the contact size effect on lattice rotation band.

3.4. Contact size effect on lattice rotation

The contact size plays a crucial role (Deshpande et al., 2007; Liu et al., 2018) as it strongly affects the plasticity introduced into the specimen. Besides the shear stress and dislocation density reported in previous sections, the localized lattice rotation band and the 'locked-in' layer, henceforth referred to as a trace line to be consistent with the experiments, are illustrated for different contact sizes in Fig. 6. As expected, a larger contact size produces a dislocation structure with a larger number of dislocations, which propagate much deeper into the indented material; this is also associated with the formation of more than one trace line. However, the location and intensity of the trace lines is nearly independent of the contact size, at least for smaller contact sizes, which correspond to smaller loads in the experiments. Of more significance, the depth from the surface of the first trace line is also independent of the contact size. This is consistent with experiments (Greiner et al., 2016).

Fig. 7 illustrates the three characteristic dimensions of the trace lines revealed in the specimen subsurface under contact size A $=$ 3.55μm, which exhibits features representative of all contact sizes. The critical depth h^* indicates the distance between the surface and the boundary between the first and second trace lines, which is independent of contact size. The critical depth is predicted by the DDP model for all contact sizes as $h^* = 0.09$ μm, which is comparable to the experimental finding of 0.1 μm (Greiner et al., 2016). This corresponds to a highly localized deformation, which is also what characterizes the depth of the plastic zone (represented as plastic slip zone), which varies as a function of the contact size and is computed to be 1.2, 3.5, 5.2 and 7.6 μm for the four contact sizes analyzed here, respectively. It has been verified that the tracelines predicted by the DDP simulation are not mesh or slip plane spacing dependent, and are not an artefact of the choice of contour levels; the mesh was fine and highly focused to the surface with a mesh size as small as $0.01\mu m$, and dislocation activity was observed between the first trace line and the contact. Both the width and height of the group of trace lines, referred to here as the lattice rotation band, labelled dl and dh, are determined by the plasticity, hence by the contact size of the preceding indentation. In the case shown here, the width of the lattice rotation band is measured as $dl = 9.5\mu m$ and the height as $dh = 6\mu m$. In the experiments the contact size was as large as $92\mu m$, much larger than in the simulations presented here (Greiner et al., 2016; Liu et al., 2018). However, as shown in Fig. 7, dl and dh scale with the contact size, therefore it is expected that the dimensions predicted by the DDP simulations would be consistent with the experimental findings for much larger contact sizes.

4. Discussion

4.1. The origin of the lattice rotation band within the subsurface

It is not yet understood how the experimentally observed dislocation trace line(s) originate from the dislocation structure induced by the sliding process (Greiner et al., 2018). In the discrete dislocation plasticity calculations (Figs. 5 and 6), the resolved shear stress is highest on the slip system parallel to the sliding direction (*i.e.* parallel to the x-axis) on the planes nearest to the surface, hence it is reasonable to anticipate that dislocation activity on these slip planes is responsible for the observed tracelines. As a result of the cohesive sliding boundary condition, the subsurface material would like to assume a simple-shear, stack-of-cards like slip arrangement (Haug et al., 2020); however compatibility with the surrounding bulk material prevents that from happening perfectly, which results in a corresponding lattice rotation. The mechanisms that the lattice rotation is given rise by accumulative dislocation glide and crystalline slip due to geometry and boundary constraints have recently been observed in other independent experimental observations including high-resolution digital image correlation (HR-DIC) (Sperry et al., 2020) and high-resolution Electron backscatter diffraction (HR-EBSD) (Maj et al., 2020), respectively.

To illustrate the origin of the dislocation traceline, the degree of rotation in the lattice rotation band is plotted versus horizontal position x for contact size A $= 1.11$ μm under a full slip condition in Fig. 9, for both vertical extents of the band identified from the lattice rotation contour plot (paths B–B′ and C–C′); the width of the lattice rotation band observed from the lattice rotation contour plot is dependent on the cut-off value that is chosen, as shown in the figure. In the inset to Fig. 9, it is evident that dislocation dipoles pile up in queues on a single horizontal slip plane underneath the contact, which are driven apart by the applied shear stress. The gradient in resolved shear stress on that slip plane – it is largest at the center of the contact and decays to zero far away from the cohesive sliding boundary condition – causes a 'soft' pile-up to form. The lattice rotation at a point on the slip plane of a single dislocation dipole is zero outside the dipole and a constant value anywhere within the dipole. Hence, theoretically, an arrangement of concentric dipoles creates a lattice rotation profile on the active slip plane that is largest at its center and decreases incrementally moving outward. This is what is

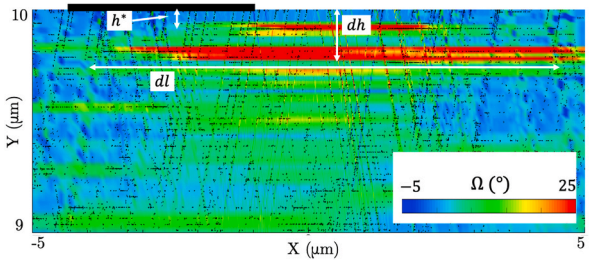

Fig. 7. Characterization of the lattice rotation band for $U = 2.76$ μm and contact size A $= 3.55$μm. The condition of full sliding has been reached.

observed in Fig. 9, where fluctuations from the theoretical trend are caused by dislocations on other slip planes.

The instantaneous dislocation structure, corresponding GND density distribution and lattice rotation distribution within the specimen for a contact size A = 1.11 μm under a full slip condition is reported in Fig. 9(a), (b) and (c), respectively. Dislocations on the horizonal slip system, which are the key contributors to the lattice rotation, are identified by a dislocation symbol that is twice as large as those on the other slip systems. Localized GND density is calculated using the net open burger's vector algorithm based on the instantaneous dislocation structure (Kiener et al., 2011). A Burgers circuit size of 25 nm was found to adequately resolve the GND distribution for these simulations. A strip of high GND density (Fig. 9(b)) is identified in the same location as the lattice rotation band, which also correlates spatially with the 'soft' pile-ups of concentric dislocation dipoles on horizontal slip planes identified here as the cause of the experimental STEM observations of dislocation tracelines (Greiner et al., 2016); furthermore, the magnitude of the predicted GND density is in line with previous measurements performed in sliding tests (Greiner et al., 2016, 2018). Regions of low lattice rotation, particularly that of the region between the lattice rotation band and the surface, referred to here as a 'locked-in' layer, also correlate with low GND density as observed in the experiments.

4.2. Comparison between STEM measurements and DDP simulation results

In the numerical results shown in Sections 3.3 and 3.4, the emergence of the experimentally observed dislocation traceline is interpreted as a result of the formation of queues of dislocation dipoles, or soft pile-ups, on slip systems parallel to the sliding direction. In this section, we compare STEM images, which show the contrast corresponding to microstructure change under sliding tests, and the lattice rotation contours obtained in the simulations. A typical comparison between experiments and simulations is illustrated in Fig. 10(a). Since the appearance of the first (uppermost) traceline is common to all indenter sizes as shown in Fig. 9, the lattice rotation is post-processed from the simulation with contact size $A = 1.11$ μm after full slip has developed and the dislocation structure has evolved to its final configuration, as this case best illustrates the mechanism responsible for the traceline and its link to lattice rotation. As mentioned previously, the simulations clearly identify a region about 0.1 μm under the contact surface where a large number of dislocation dipoles glide parallel to the surface, and a corresponding layer above it which is 'locked-in' and does not deform appreciably. The lattice rotation along three vertical paths (defined in (a)) originating at the contact face are shown in Fig. 10(b). A significant peak indicating very large lattice rotation is observed about 0.1 μm from the contact surface. This peak diminishes moving from the contact center (the blue path) towards the contact edge (the green path), which reflects the results in Fig. 8. The vertical distribution of lattice rotation divides the material into three layers, moving from the contact face into the bulk. These are: a rotation-constrained zone, a region with significant lattice rotation (due to soft pile-ups of dislocations on horizontal slip planes) and a remote zone that is unaffected by the sliding. This dislocation configuration in conjunction with the contact constraint induces large localized lattice rotation, interpreted physically as a line (in fact, a very thin layer of material) parallel to the sliding direction across which there is an abrupt change of microstructure, as observed in the experiments. This is in strong agreement with the evidence provided by the companion paper that the misorientation is concentrated at the DTL (see e.g. Fig. 6 of (Ruebeling et al., 2021) and related discussion). This magnitude of the characteristic length is system specific and we believe is linked to the combined effect of the cohesive strength (i.e. maximum shear stress), Burger's vector and other material properties (moduli, plastic flow stress) used to describe the specific systems under investigation. The nature of the load and the contact size affect the behavior (and the relative lattice rotation/deformation) of the material above and below the DTL, as discussed below in more details.

The critical depth of the 1st DTL obtained from the simulations (0.1 μm) agrees very well with the experimental findings, albeit the contact size in the two was different but this feature was shown in the simulations to be contact-size independent; the dislocation activity under the indenter is strictly controlled by the pressure and the shear traction transmitted across the interface, which is an approximate match between the simulations and the values experienced by the material layer under low loads in the experiments. Changing the size of the indenter changes the extent of the material affected by large stresses rather than the value in the uppermost layer of the material. The features shown in Fig. 10 are common to all other indentation sizes but extend further into the specimens for larger indenters, with the emergence of other tracelines (as also shown in the experiments) further away from the surface. The

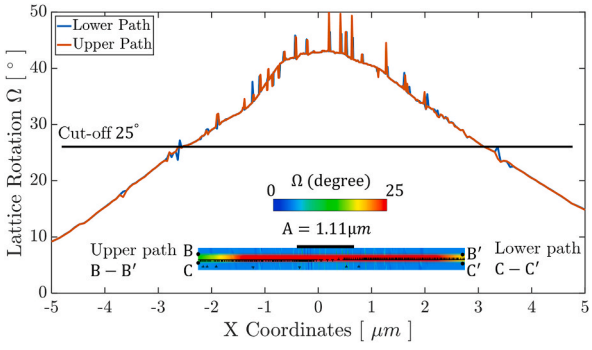

Fig. 8. Lattice rotation on a horizontal slip plane within the subsurface. Results are shown when full slip is achieved for contact size A = 1.11 μm (see Fig. 6a).

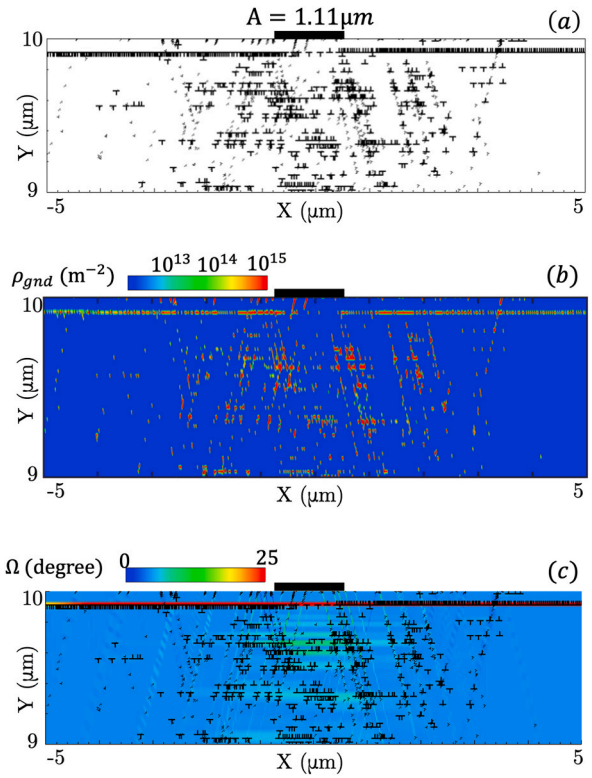

Fig. 9. Correlation between (a) the instantaneous distribution of dislocations, (b) the corresponding geometrically necessary dislocation (GND) density distribution and (c) lattice rotation using the discrete dislocation plasticity model. Numerical results are extracted when full sliding occurs under contact size A = 1.11μm (see Fig. 6a). Dislocation symbol size is enlarged for dislocations along the horizontal slip planes.

dislocation activity becomes more complex when the indenter size (and hence the overall load since the pressure on the indenter in the experiments is kept constant) grows due to the activation of a large number of dislocations along different slip systems and slip planes. This usually results in progressive material rotation between tracelines (i.e. bands increasing in lattice rotation between consecutive DTLs), with the largest lattice rotation experienced by the plastically deformed material further away from the contact; this is due to the fact that this region, which one can associate with the bulk material (see Fig. 6), in not constrained by the indenter and lattice rotation exhibits itself differently in this region. This explains not only why the number of DTLs and the lattice rotation increase with the size of the indenter, but also why large contact areas (typical of the experiments under consideration) result is large lattice rotations recorded beneath the last observable DTL, as the reach of the plastically deformed area is much deeper than the area analyzed by STEM. A further interesting point to discuss is that increasing the load leads to more severe microstructural changes, which include increased (geometrically necessary) dislocation activity (and hence damage(Lu et al., 2020)) and the formation of small grains and re-crystallization in the tribologically affected layer. The simulations in Fig. 6(d) (largest indenter size studied here) already show very large dislocation activity on different slip systems. It can be inferred that a large contact size and normal load may lead to the subsequent formation of new grain boundaries GND density that have been characterized in previous experiments (Greiner et al., 2016).

4.3. Comparison between TKD measurements and DDP simulation results

The qualitative comparison between the STEM image and the lattice rotation contours in Fig. 10 has shown the strong correlation between the perceived abrupt microstructural changes in the experiments and the material lattice rotation under sliding conditions. We turn now to quantitative measurements using Transmission Kikuchi Diffraction (TKD), which have been used to determine lattice rotation in the neighborhoods of the DTLs in (Ruebeling et al., 2021).

The lattice rotation within the specimen calculated using DDP and measured using TKD is illustrated in Fig. 11 (a) and (b), respectively. The numerical results in Fig. 11 (a) are obtained from simulations under the maximum contact size (A = 95 μm) achieved in the DDP calculations, which is the closest match possible between the two systems given the computational demands of DDP. The subsurface region under the indenter is subjected to a similar stress state. However, the size of the indenter used in the simulation is still smaller than the contact area for the equivalent experiment, hence the region of material over which high stresses and strains are calculated is not as deep as the equivalent region in the experimental test. The A = 95 μm simulation is nonetheless sufficient to accurately capture the lattice rotation band parallel to the sliding direction underneath the contact, which is also observed in the TKD experimental results shown in Fig. 11(b). In addition, the lattice rotation map predicted by the DDP simulations exhibits several thin

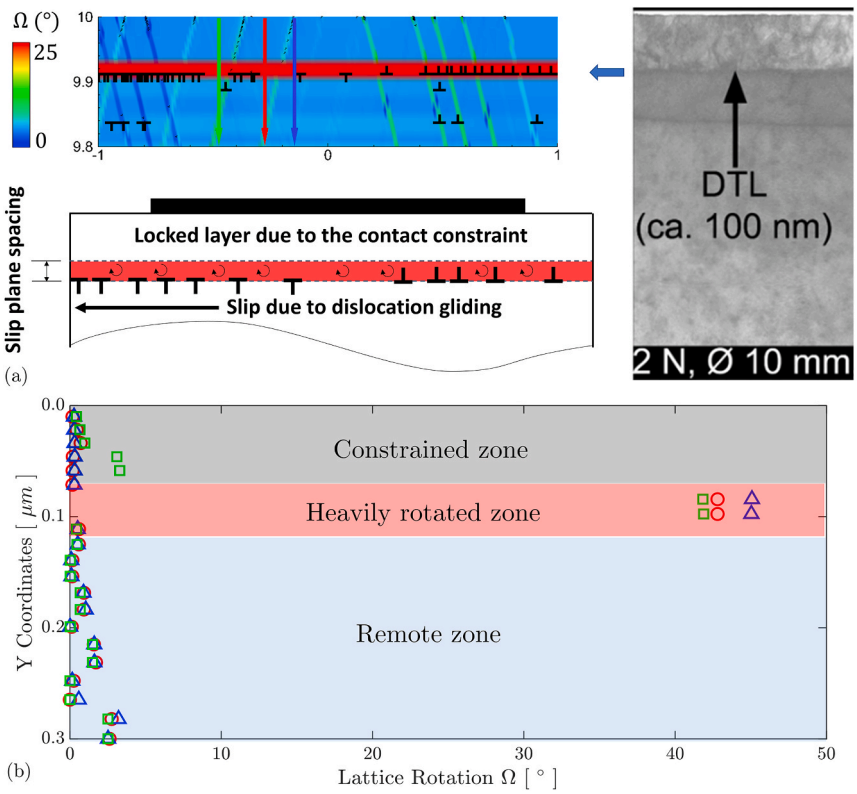

Fig. 10. (a) Comparison between the STEM image obtained from experiments for low loads (shown on the right, zoomed-in from Fig. 6a) and the lattice rotation and superimposed dislocation structure computed via DDP simulations (shown on the top-left, zoomed-in from Fig. 9a), highlighting the dislocation activity linked to the mechanism responsible for the lattice rotation and formation of the traceline. This is also schematically depicted at the bottom-left, showing the (b) lattice rotation distribution along three paths (defined in (a)) perpendicular to the sliding direction. Results are shown at the instant when the sliding has been initiated and dislocation motion has developed in the slip systems underneath the contact.

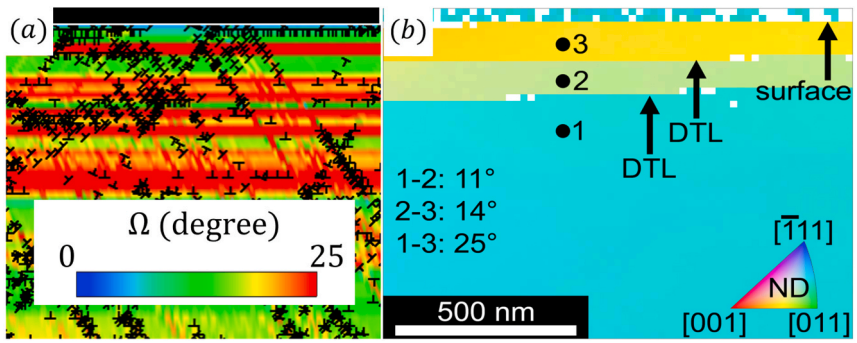

Fig. 11. The comparison between (a) lattice rotation evaluated in DDP simulations with superimposed instantaneous dislocation structure and (b) lattice rotation measured using the TKD pattern. Numerical results are shown for full slip and contact size A = 95μm, when dislocation motion and lattice rotation have reached their final stable configuration. The simulation set-up is the closest possible scenario to replicate the one-stroke sliding tests.

strips with a limited lattice rotation compared to that in adjacent regions, which separate the lattice rotation band from the subsurface. The separation lines are again interpreted as tracelines (*i.e.* the discontinuity discussed in Section 4.1), and the depths of the first two tracelines are similar to those observed in the TKD pattern map. The DDP simulations not only exhibit a similar lattice rotation pattern, but the predictions also appear to be quantitatively commensurate with the magnitude of misorientation measured experimentally between different material strips shown in Fig. 11(b). For instance, the lattice rotation within the most severely rotated material strip is roughly $\Omega = 30^\circ$ in the DDP calculations, whereas the relative misorientation measured using TKD between the surface and the region below the second traceline is $\Omega = 25^\circ$. The calculated lattice rotation and misorientation measurement in the other two layers show the

same trend. In Section 3.4, we have shown the positive dependence of the lattice rotation band dimensions on the contact size. The depth of the heavily rotated material enlarges with the contact size and the lattice rotation in the simulations does not extend to the full region shown in Fig. 11(b) due to the limited contact size used for the simulation. In the experiment the material below the second (lowest) DTL shows large rotation deeper into the substrate (see Fig. 11(b)) as the contact size is substantially larger than the field of view in STEM (about one micrometre).

5. Conclusion

Discrete dislocation plasticity analyses have been conducted to simulate the dislocation structure and localized lattice rotation under single asperity sliding, where the contact between the asperity and specimen was established by a preceding sinusoidal indentation. This was done to interpret the dislocation tracelines observed in corresponding experiments. The following conclusions are highlighted:

(i) The entire sliding process up until full slip occurs is divided into three regimes by sliding distance, where the two critical sliding distances demarcating these regimes are identified from the shear stress and dislocation density response. Both of the critical distances are found to be strongly contact size dependent.
(ii) The “dislocation traceline”, characterized by an abrupt contrast change observed in the STEM images obtained after the first sliding stroke, is due to a highly localized lattice rotation band within the material subsurface and parallel to the sliding direction; this localized response emerges with increasing sliding distance and is dependent upon the contact size. The lattice rotation arises as a result of the deformation induced by the appearance and evolution of a pattern of concentric dislocation dipoles in conjunction with the compatibility constraint of the surrounding material and the applied contact condition at the surface.
(iii) The critical depth from the contact to the top boundary of the horizontal lattice rotation band predicted by the DDP calculations shows excellent agreement with the experimental measurements. Contact size and the corresponding total normal load do not affect the critical depth of the initial traceline, yet these parameters dominate the width and depth of the lattice band when full slip occurs. This finding provides mechanistic insight into the damage development and subgrain formation observed in tests when larger loads are applied, which have not been explicitly modelled in this contribution.
(iv) A very good agreement was observed between the predicted lattice rotation magnitude and the experimentally measured misorientation between subsurface layers.

Author statement

Yilun Xu: Methodology, Software, Original draft preparation, Visualization.
Friederike Ruebeling: Investigation, Experiments, Visualization.
Daniel.S. Balint: Methodology, Writing- Reviewing and Editing.
Christian Greiner: Conceptualization, Writing- Reviewing and Editing.
Daniele Dini: Conceptualization, Methodology, Writing- Reviewing and Editing.

Declaration of competing interest

The authors declare that they have no known competing financial interests or personal relationships that could have appeared to influence the work reported in this paper.

Acknowledgment

YX and DD would like to acknowledge funding from the EPSRC through the Established Career Fellowship grant (EP/N025954/1). CG acknowledges funding the European Research Council (ERC) under Grant No. 771237 (TriboKey).

Appendix A. Supplementary data

Supplementary data to this article can be found online at https://doi.org/10.1016/j.ijplas.2021.102942.

Appendix

Lattice rotation validation for indentation (Supplement to Section 2.3)

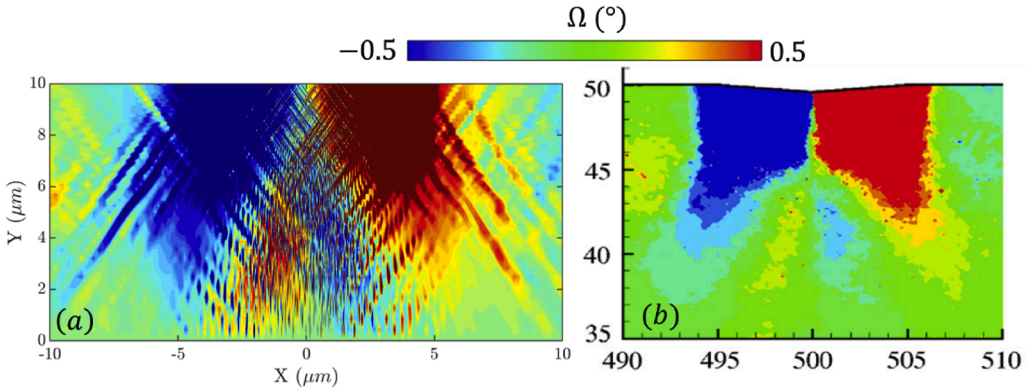

Fig. A 1. Lattice rotation validation for indentation. Lattice rotation distribution in indentation of (a) the sinusoidal indenter adopted in this research (b) a wedge-shaped indenter with similar geometric characteristics studied in (Zhang et al., 2014). The result is shown at the instant when the same indentation depth $\delta = 0.4$ μm is imposed on both indenters, respectively.

Material properties

Table 1
Material properties in DDP modelling

Parameter Name	Symbol	Unit	Value
Young's modules	E	GPa	70
Poisson ratio	υ	–	0.33
Burger's vector	b	nm	0.25
Spacing of slip planes	–	b	100
Drag coefficient	B	Pa · s	10^{-4}
Annihilation distance	L_e	b	6
Mean source strength	$\overline{\tau}_{nuc}$	MPa	50
Obstacle strength	τ_{obs}	MPa	150
Source density	ρ_{nuc}	μm^{-2}	40
Obstacle density	ρ_{obs}	μm^{-2}	80

References

Akarapu, S., Zbib, H.M., Bahr, D.F., 2010. Analysis of heterogeneous deformation and dislocation dynamics in single crystal micropillars under compression. Int. J. Plast. 26, 239–257. https://doi.org/10.1016/j.ijplas.2009.06.005.

Arsenlis, A., Parks, D.M., 1999. Crystallographic aspects of geometrically-necessary and statistically-stored dislocation density. Acta Mater. 47, 1597–1611. https://doi.org/10.1016/S1359-6454(99)00020-8.

Balint, D.S., Deshpande, V.S., Needleman, A., Van der Giessen, E., 2005. A discrete dislocation plasticity analysis of grain-size strengthening. Mat Sci Eng a-Struct 400, 186–190. https://doi.org/10.1016/j.msea.2005.02.082.

Balint, D.S., Deshpande, V.S., Needleman, A., Van der Giessen, E., 2006a. Discrete dislocation plasticity analysis of the wedge indentation of films. J. Mech. Phys. Solid. 54, 2281–2303. https://doi.org/10.1016/j.jmps.2006.07.004.

Balint, D.S., Deshpande, V.S., Needleman, A., Van der Giessen, E., 2006b. Size effects in uniaxial deformation of single and polycrystals: a discrete dislocation plasticity analysis. Model Simul Mater Sc 14, 409–422. https://doi.org/10.1088/0965-0393/14/3/005.

Balint, D.S., Deshpande, V.S., Needleman, A., Van der Giessen, E., 2008. Discrete dislocation plasticity analysis of the grain size dependence of the flow strength of polycrystals. Int. J. Plast. 24, 2149–2172. https://doi.org/10.1016/j.ijplas.2007.08.005.

Benzerga, A.A., 2008. An analysis of exhaustion hardening in micron-scale plasticity. Int. J. Plast. 24, 1128–1157. https://doi.org/10.1016/j.ijplas.2007.08.010.

Bertin, N., Sills, R.B., Cai, W., 2020. Frontiers in the simulation of dislocations. Annu. Rev. Mater. Res. 50, 437–464. https://doi.org/10.1146/annurev-matsci-091819015500, 2020 50.

Bouvier, S., Needleman, A., 2006. Effect of the number and orientation of active slip systems on plane strain single crystal indentation. Model Simul Mater Sc 14, 1105–1125. https://doi.org/10.1088/0965-0393/14/7/001.

Cheng, J.H., Ghosh, S., 2015. A crystal plasticity FE model for deformation with twin nucleation in magnesium alloys. Int. J. Plast. 67, 148–170. https://doi.org/10.1016/j.ijplas.2014.10.005.

Chenje, T.W., Simbi, D.J., Navara, E., 2004. Relationship between microstructure, hardness, impact toughness and wear performance of selected grinding media for mineral ore milling operations. Mater. Des. 25, 11–18. https://doi.org/10.1016/S0261-3069(03)00168-7.

Cheong, K.S., Busso, E.P., Arsenlis, A., 2005. A study of microstructural length scale effects on the behaviour of FCC polycrystals using strain gradient concepts. Int. J. Plast. 21, 1797–1814. https://doi.org/10.1016/j.ijplas.2004.11.001.

Counts, W.A., Braginsky, M.V., Battaile, C.C., Holm, E.A., 2008. Predicting the Hall-Petch effect in fcc metals using non-local crystal plasticity. Int. J. Plast. 24, 1243–1263. https://doi.org/10.1016/j.ijplas.2007.09.008.

Das, S., Hofmann, F., Tarleton, E., 2018. Consistent determination of geometrically necessary dislocation density from simulations and experiments. Int. J. Plast. 109, 18–42. https://doi.org/10.1016/j.ijplas.2018.05.001.

Deshpande, V.S., Balint, D.S., Needleman, A., Van der Giessen, E., 2007. Size effects in single asperity frictional contacts. Model Simul Mater Sc 15, S97–S108. https://doi.org/10.1088/0965-0393/15/1/S09.
Deshpande, V.S., Needleman, A., Van der Giessen, E., 2004. Discrete dislocation plasticity analysis of static friction. Acta Mater. 52, 3135–3149. https://doi.org/10.1016/j.actamat.2004.03.018.
Deshpande, V.S., Needleman, A., Van der Giessen, E., 2005. Plasticity size effects in tension and compression of single crystals. J. Mech. Phys. Solid. 53, 2661–2691. https://doi.org/10.1016/j.jmps.2005.07.005.
Dunne, F.P.E., Rugg, D., Walker, A., 2007a. Lengthscale-dependent, elastically anisotropic, physically-based hcp crystal plasticity: application to cold-dwell fatigue in Ti alloys. Int. J. Plast. 23, 1061–1083. https://doi.org/10.1016/j.ijplas.2006.10.013.
Dunne, F.P.E., Wilkinson, A.J., Allen, R., 2007b. Experimental and computational studies of low cycle fatigue crack nucleation in a polycrystal. Int. J. Plast. 23, 273–295. https://doi.org/10.1016/j.ijplas.2006.07.001.
El Ters, P., Shehadeh, M.A., 2019. Modeling the temperature and high strain rate sensitivity in BCC iron: atomistically informed multiscale dislocation dynamics simulations. Int. J. Plast. 112, 257–277. https://doi.org/10.1016/j.ijplas.2018.09.002.
Greiner, C., Liu, Z., Strassberger, L., Gumbsch, P., 2016. Sequence of stages in the microstructure evolution in copper under mild reciprocating tribological loading. ACS Appl. Mater. Interfaces 8, 15809–15819. https://doi.org/10.1021/acsami.6b04035.
Greiner, C., Liu, Z.L., Schneider, R., Pastewka, L., Gumbsch, P., 2018. The origin of surface microstructure evolution in sliding friction. Scripta Mater. 153, 63–67. https://doi.org/10.1016/j.scriptamat.2018.04.048.
Gurrutxaga-Lerma, B., Shehadeh, M.A., Balint, D.S., Dini, D., Chen, L., Eakins, D.E., 2017. The effect of temperature on the elastic precursor decay in shock loaded FCC aluminium and BCC iron. Int. J. Plast. 96, 135–155. https://doi.org/10.1016/j.ijplas.2017.05.001.
Gurrutxaga–Lerma, B., Verschueren, J., Sutton, A.P., Dini, D., 2020. The mechanics and physics of high-speed dislocations: a critical review. Int. Mater. Rev. 1–41. https://doi.org/10.1080/09506608.2020.1749781.
Hattori, T., Kaneko, Y., Hashimoto, S., 2008. Wear-induced microstructure in Ni/Cu nano-multilayers. J. Mater. Sci. 43, 3923–3930. https://doi.org/10.1007/s10853-007-2372-5.
Haug, C., Ruebeling, F., Kashiwar, A., Gumbsch, P., Kubel, C., Greiner, C., 2020. Early deformation mechanisms in the shear affected region underneath a copper sliding contact. Nat. Commun. 11, 839. https://doi.org/10.1038/s41467-020-14640-2.
Hirth, J.P., Lothe, J., 1982. Theory of Dislocations.
Hughes, D.A., Hansen, N., 2001. Graded nanostructures produced by sliding and exhibiting universal behavior. Phys. Rev. Lett. 87, 135503. https://doi.org/10.1103/PhysRevLett.87.135503.
Johnson, K.L., 1997. Adhesion and friction between a smooth elastic spherical asperity and a plane surface. P Roy Soc a-Math Phy 453, 163–179. https://doi.org/10.1098/rspa.1997.0010.
Karthikeyan, S., Agrawal, A., Rigney, D.A., 2009. Molecular dynamics simulations of sliding in an Fe-Cu tribopair system. Wear 267, 1166–1176. https://doi.org/10.1016/j.wear.2009.01.032.
Kiener, D., Guruprasad, P.J., Keralavarma, S.M., Dehm, G., Benzerga, A.A., 2011. Work hardening in micropillar compression: in situ experiments and modeling. Acta Mater. 59, 3825–3840. https://doi.org/10.1016/j.actamat.2011.03.003.
Kuksenko, V., Roberts, S., Tarleton, E., 2019. The hardness and modulus of polycrystalline beryllium from nano-indentation. Int. J. Plast. 116, 62–80. https://doi.org/10.1016/j.ijplas.2018.12.008.
Kysar, J.W., Saito, Y., Oztop, M.S., Lee, D., Huh, W.T., 2010. Experimental lower bounds on geometrically necessary dislocation density. Int. J. Plast. 26, 1097–1123. https://doi.org/10.1016/j.ijplas.2010.03.009.
Lewandowski, M.J., Stupkiewicz, S., 2018. Size effects in wedge indentation predicted by a gradient-enhanced crystal-plasticity model. Int. J. Plast. 109, 54–78. https://doi.org/10.1016/j.ijplas.2018.05.008.
Liu, Z.L., Patzig, C., Selle, S., Hoche, T., Gumbsch, P., Greiner, C., 2018. Stages in the tribologically-induced oxidation of high-purity copper. Scripta Mater. 153, 114–117. https://doi.org/10.1016/j.scriptamat.2018.05.008.
Lu, S.J., Zhang, B., Li, X.Y., Zhao, J.W., Zaiser, M., Fan, H.D., Zhang, X., 2019. Grain boundary effect on nanoindentation: a multiscale discrete dislocation dynamics model. J. Mech. Phys. Solid. 126, 117–135. https://doi.org/10.1016/j.jmps.2019.02.003.
Lu, X., Dunne, F.P.E., Xu, Y., 2020. A crystal plasticity investigation of slip system interaction, GND density and stored energy in non-proportional fatigue in Nickel-based superalloy. Int. J. Fatig. 139, 105782. https://doi.org/10.1016/j.ijfatigue.2020.105782.
Maj, M., Nowak, M., Musial, S., Plocinski, T., 2020. Experimental analysis of material, lattice and plastic rotation during deformation of aluminium multicrystal. Mat Sci Eng a-Struct 790, 139725. https://doi.org/10.1016/j.msea.2020.139725.
Meissonnier, F.T., Busso, E.P., O'Dowd, N.P., 2001. Finite element implementation of a generalised non-local rate-dependent crystallographic formulation for finite strains. Int. J. Plast. 17, 601–640. https://doi.org/10.1016/S0749-6419(00)00064-4.
Menga, N., Carbone, G., Dini, D., 2018. Do uniform tangential interfacial stresses enhance adhesion? J. Mech. Phys. Solid. 112, 145–156. https://doi.org/10.1016/j.jmps.2017.11.022.
Motz, C., Weygand, D., Senger, J., Gumbsch, P., 2008. Micro-bending tests: a comparison between three-dimensional discrete dislocation dynamics simulations and experiments. Acta Mater. 56, 1942–1955. https://doi.org/10.1016/j.actamat.2007.12.053.
Nix, W.D., Gao, H.J., 1998. Indentation size effects in crystalline materials: a law for strain gradient plasticity. J. Mech. Phys. Solid. 46, 411–425. https://doi.org/10.1016/S0022-5096(97)00086-0.
Pastewka, L., Moser, S., Gumbsch, P., Moseler, M., 2011. Anisotropic mechanical amorphization drives wear in diamond. Nat. Mater. 10, 34–38. https://doi.org/10.1038/nmat2902.
Peng, B., Li, Q., Feng, X.-Q., Gao, H., 2021. Effect of shear stress on adhesive contact with a generalized Maugis-Dugdale cohesive zone model. J. Mech. Phys. Solid. 148 https://doi.org/10.1016/j.jmps.2020.104275.
Pharr, G.M., Herbert, E.G., Gao, Y.F., 2010. The indentation size effect: a critical examination of experimental observations and mechanistic interpretations. Annu. Rev. Mater. Res. 40, 271–292. https://doi.org/10.1146/annurev-matsci-070909-104456.
Po, G., Huang, Y., Ghoniem, N., 2019. A continuum dislocation-based model of wedge microindentation of single crystals. Int. J. Plast. 114, 72–86. https://doi.org/10.1016/j.ijplas.2018.10.008.
Prastiti, N.G., Xu, Y.L., Balint, D.S., Dunne, F.P.E., 2020. Discrete dislocation, crystal plasticity and experimental studies of fatigue crack nucleation in single-crystal nickel. Int. J. Plast. 126 https://doi.org/10.1016/j.ijplas.2019.10.003.
Qu, S., Huang, Y., Pharr, G.M., Hwang, K.C., 2006. The indentation size effect in the spherical indentation of iridium: a study via the conventional theory of mechanism-based strain gradient plasticity. Int. J. Plast. 22, 1265–1286. https://doi.org/10.1016/j.ijplas.2005.07.008.
Rigney, D.A., Glaeser, W.A., 1978. Significance of near-surface microstructure in wear process. Wear 46, 241–250. https://doi.org/10.1016/0043-1648(78)90125-4.
Rigney, D.A., Hirth, J.P., 1979. Plastic-deformation and sliding friction of metals. Wear 53, 345–370. https://doi.org/10.1016/0043-1648(79)90087-5.
Ruebeling, F., Xu, Y., Richter, G., Dini, D., Gumbsch, P., Greiner, C., 2021. Normal load and counter body size influence the initiation of microstructural discontinuities in copper during sliding. ACS Appl. Mater. Interfaces. https://doi.org/10.1021/acsami.0c19736.
Saraev, D., Miller, R.E., 2006. Atomic-scale simulations of nanoindentation-induced plasticity in copper crystals with nanometer-sized nickel coatings. Acta Mater. 54, 33–45. https://doi.org/10.1016/j.actamat.2005.08.030.
Song, H., Deshpande, V.S., Van der Giessen, E., 2016. Discrete dislocation plasticity analysis of loading rate-dependent static friction. Proc. Math. Phys. Eng. Sci. 472, 20150877. https://doi.org/10.1098/rspa.2015.0877.
Sperry, R., Harte, A., da Fonseca, J.Q., Homer, E.R., Wagoner, R.H., Fullwood, D.T., 2020. Slip band characteristics in the presence of grain boundaries in nickel-based superalloy. Acta Mater. 193, 229–238. https://doi.org/10.1016/j.actamat.2020.04.037.
Stoyanov, P., Romero, P.A., Merz, R., Kopnarski, M., Stricker, M., Stemmer, P., Dienwiebel, M., Moseler, M., 2014. Nano scale sliding friction phenomena at the interface of diamond-like carbon and tungsten. Acta Mater. 67, 395–408. https://doi.org/10.1016/j.actamat.2013.12.029.

Tarleton, E., Balint, D.S., Gong, J., Wilkinson, A.J., 2015. A discrete dislocation plasticity study of the micro-cantilever size effect. Acta Mater. 88, 271–282. https://doi.org/10.1016/j.actamat.2015.01.030.

Van der Giessen, E., Needleman, A., 1995. Discrete dislocation plasticity - a simple planar model. Model Simul Mater Sc 3, 689–735.

van der Giessen, E., Schultz, P.A., Bertin, N., Bulatov, V.V., Cai, W., Csányi, G., Foiles, S.M., Geers, M.G.D., González, C., Hütter, M., Kim, W.K., Kochmann, D.M., Llorca, J., Mattsson, A.E., Rottler, J., Shluger, A., Sills, R.B., Steinbach, I., Strachan, A., Tadmor, E.B., 2020. Roadmap on multiscale materials modeling. Model Simul Mater Sc 28, 043001. https://doi.org/10.1088/1361-651X/ab7150.

Widjaja, A., Van der Giessen, E., Deshpande, V.S., Needleman, A., 2007a. Contact area and size effects in discrete dislocation modeling of wedge indentation. J. Mater. Res. 22, 655–663. https://doi.org/10.1557/Jmr.2007.0090.

Widjaja, A., Van der Giessen, E., Needleman, A., 2007b. Discrete dislocation analysis of the wedge indentation of polycrystals. Acta Mater. 55, 6408–6415. https://doi.org/10.1016/j.actamat.2007.07.053.

Xu, Y., Balint, D.S., Dini, D., 2016. A method of coupling discrete dislocation plasticity to the crystal plasticity finite element method. Model Simul Mater Sc 24, 045007. https://doi.org/10.1088/0965-0393/24/4/045007.

Xu, Y., Balint, D.S., Dini, D., 2019. A new hardness formula incorporating the effect of source density on indentation response: a discrete dislocation plasticity analysis. Surf. Coating. Technol. 374, 763–773. https://doi.org/10.1016/j.surfcoat.2019.06.045.

Xu, Y., Joseph, S., Karamched, P., Fox, K., Rugg, D., Dunne, F.P.E., Dye, D., 2020. Predicting dwell fatigue life in titanium alloys using modelling and experiment. Nat. Commun. 11, 5868. https://doi.org/10.1038/s41467-020-19470-w.

Zhang, M., Neu, R.W., McDowell, D.L., 2009. Microstructure-sensitive modeling: application to fretting contacts. Int. J. Fatig. 31, 1397–1406. https://doi.org/10.1016/j.ijfatigue.2009.03.023.

Zhang, Y.H., Gao, Y.F., Nicola, L., 2014. Lattice rotation caused by wedge indentation of a single crystal: dislocation dynamics compared to crystal plasticity simulations. J. Mech. Phys. Solid. 68, 267–279. https://doi.org/10.1016/j.jmps.2014.04.006.